

Flexible control of highly-directive emissions based on bifunctional metasurfaces with low polarization cross-talking

He-Xiu Xu^{1,2,*}, Shiwei Tang³, Xiaohui Ling¹, Weijie Luo¹, and Lei Zhou^{1,*}

Received 23 January 2017, revised 21 February 2017, accepted 21 February 2017

Published online 14 March 2017

Achieving flexible and highly directive emissions toward pre-designed directions has intrigued long-held interest in both science and engineering community, but most available efforts suffer the issues of bulky size, limited functionalities, and low efficiency. Here, we propose a general strategy to *efficiently* and flexibly control the emission beams with dual functionalities realized independently by orthogonal excitations. To overcome the polarization cross-talking, a novel planar multi-mode anisotropic meta-atom is designed by incorporating the screening effect of a surrounding wire loop. As the result, we can design the polarization-dependent phase profile under certain polarization, without worrying about their influences on the other polarization. As an illustration, two proof-of-concept metasurfaces are actualized at microwave frequencies, of which one combines the functionalities of focused-beam and large-angle multibeam emissions while another hybrids the functionalities of beam-steering and small-angle multibeam emissions. Theoretical, full-wave simulation, and experimental results are in excellent agreement with each other, which collectively demonstrate the desired performances of our bifunctional devices. Our proposed strategy paves the way to realize high-performance multifunctional optical devices with high integration and complex wavefront manipulations.

1 Introduction

Highly directive emissions with flexible beam numbers and beam directions are highly desirable in modern smart communication systems. This is especially true

for the multiple pencil beams with arbitrary directions which have intrigued numerous applications such as direct broadcasting, satellite communications, multiple target radars, SAR, MIMO and surveillance systems. Available strategies to achieve such target include using zero-refractive-index metamaterials [1–3] and gradient-refractive-index metamaterials [4–6]. Though pencil beam was realized with high gain, the whole emission systems featured bulky, lossy, high cost and posed difficult fabrication challenges. Metasurfaces, planar versions of metamaterials [7, 8], have recently attracted significant interest in both science and engineering community, since they exhibited unprecedented control capabilities on electromagnetic (EM) waves and overcame certain drawbacks of bulk metamaterials. Via manipulating the abrupt phase discontinuities on the metasurfaces, researchers have demonstrated the generalized laws of reflection/refraction [8], high-efficiency conversion of propagating wave (PW) to surface wave (SW) [9], and other fascinating effects [10, 11]. Accompanying the phase control, independent control on the magnitudes of waves scattered from different meta-atoms was also implemented to realize more sophisticated wavefront manipulations [12, 13]. The concept of coding metasurface was also proposed to control EM waves by performing digital signal processing [14]. Recently, an elegant strategy was proposed to overcome the

* Corresponding authors: E-mail: phzhou@fudan.edu.cn, hxxuellen@gmail.com

¹ State Key Laboratory of Surface Physics, Key Laboratory of Micro and Nano Photonic Structures (Ministry of Education), Collaborative Innovation Center of Advanced Microstructures, and Physics Department of Fudan University, Shanghai 200433, China

² Air and Missile Defense College, Air Force Engineering University, Xi'an 710051, China

³ Department of Physics, Faculty of Science, Ningbo University, Ningbo 315211, China

functionality variations in the frequency response of metasurfaces caused by the dispersion of the meta-atoms [15]. Many applications were demonstrated based on metasurfaces, such as broadband anomalous reflection/refraction [16–20], flat lensing [21–24], quarter-wave plate [25], vortex-beam generation [26, 27], surface plasmon couplers [28], metamirrors [29] and holograms [30–32].

On the other hand, much attention was paid to metasurfaces constructed by anisotropic meta-atoms which possess polarization-dependent capabilities to control the EM wavefronts [33–40]. Unfortunately, most metasurfaces realized so far exhibit identical/similar functionalities (say, anomalous beam steering) for different incident polarizations [33–35]. Moreover, the adopted anisotropic meta-atoms (nano-bricks or I-shaped structures) exhibit undesired polarization cross-talking which are inconvenient for fast designs of bifunctional meta-devices, since changing one parameter of the meta-atom can influence the functionalities related to both polarizations. Such issue is more severe for designing meta-devices with more complex functions, which typically require two-dimensional (2D) parameter searching to realize the desired phase profiles for two polarizations. This distinguished from aforementioned beam steering which only requires one-dimensional (1D) structure variations for each polarization. Although polarization-controlled dual-beam and diffusion-beam scatterings were recently integrated in one single plate using coding methods, significant normal reflections and asymmetric amplitude were observed in dual-beam channel [39]. Meanwhile, holographic metasurface was utilized to realize double-beam radiations based on isotropic meta-atoms [41], but the emissions cannot be flexibly controlled and require simultaneous two excitations. In analogue to metasurfaces in terms of spatial phase control, reflectarrays/transmitarrays were overwhelmingly investigated in conventional EM community to realize high-gain focused beam, steering beam and multiple pencil beams [42–44]. We note that the beam steering realized by active devices such as diodes may induce large power loss and worsened gain, and the parasitic radiation arising from the bias lines also degrades the performance. Most importantly, the commonly utilized nano rods exhibits undesired polarization cross-talking which hinders the hybrid functionality integration. To date, combining two aforementioned emission functionalities in a single array is rarely seen.

Here, we propose a strategy to *efficiently* design a bifunctional metasurface, by adopting a carefully designed anisotropic meta-atom exhibiting low polarization cross-talking. Different from the beam

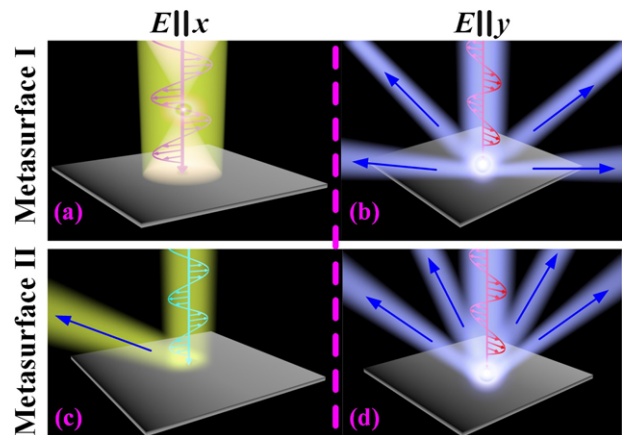


Figure 1 Schematic illustration and working principle of two flexible emission systems based on two bifunctional metasurfaces. (a, b) For emission system I, the metasurface functions as (a) a lens to focus the beam and (b) a beam splitter to generate quad large-angle pencil beams with polarizations $E||x$ and $E||y$, respectively. (c, d) For emission system II, the metasurface functions as (c) a beam deflector to steering the beam and (d) a beam splitter to generate quad small-angle pencil beams with polarizations $E||x$ and $E||y$, respectively.

splitting based on generalized Snell' law [39], the multi-beam radiations were realized with very low sidelobes and symmetric amplitudes based on array theory and elegant optimizations. The big difference between metasurfaces and reflectarrays/transmitarrays is the deeply subwavelength-scale meta-atoms employed in the former case which are capable of notably relaxing the sensitivity and effects of large-angle oblique incidence to emissions. We designed and fabricated two proof-of-concept meta-devices, each combining two distinct complex functionalities including steered-beam, focused-beam and multi-beam directional emissions (see Fig. 1). In both cases, the complicated phase profiles for two distinct functionalities require 2D geometrical-parameter searching and thus our strategy can save lots of time in designing such devices. The flexibly-controlled highly directive emissions with multifunctionalities have huge fascinations and prospects to conveniently integrate complex systems with low costs.

2 Strategy for low polarization-crosstalking

For an arbitrary anisotropic metasurface under the Cartesian coordinate system, we require four variables to describe the phase gradients $\xi_x(x)$, $\xi_y(x)$, $\xi_x(y)$ and $\xi_y(y)$

along different directions under different polarizations,

$$\begin{bmatrix} \xi_x(x) & \xi_y(x) \\ \xi_x(y) & \xi_y(y) \end{bmatrix} = \begin{bmatrix} \frac{\partial \varphi_x(x, y)}{\partial x} & \frac{\partial \varphi_y(x, y)}{\partial y} \\ \frac{\partial \varphi_x(x, y)}{\partial x} & \frac{\partial \varphi_y(x, y)}{\partial y} \end{bmatrix} \quad (1)$$

Here x or y in the subscript of $\xi_x(x)$, $\xi_y(x)$, $\xi_x(y)$ and $\xi_y(y)$ denotes the gradient direction, whereas that in the bracket represents the polarization direction. We thus have four degrees of freedom to describe and design anisotropic metasurface. According to the generalized Snell's law, the transverse (k_x and k_y) and longitudinal (k_z) wave vectors of the EM wave scattered by the metasurface (shined by a normally incident EM wave) are given by

$$\begin{cases} k_x(x/y) = \xi_x(x/y) \\ k_y(x/y) = \xi_y(x/y) \\ k_z(x/y) = \sqrt{k_0^2 - k_x^2(x/y) - k_y^2(x/y)} \end{cases} \quad (2)$$

Eq. (2) shows that the wave-vector of the scattered EM wave can be controlled by both the incident polarization and the related phase gradient. These expanded freedoms are extremely helpful to achieve diversified EM characteristics. In practice, one typically obtains the desired $\xi_x(\sigma)$ and $\xi_y(\sigma)$ properties through changing the geometrical parameters of the meta-atom which are sensitive to the σ -polarized EM wave. However, for many meta-atoms with polarization cross-talking, the variation of structural parameters along the x direction often strongly affects the phase gradients/profiles related to the y -polarization, and thus making it hard (if not impossible) to realize an accurate and fast design for the four gradients simultaneously.

To address above issue, we design a meta-atom exhibiting nearly negligible polarization cross-talking, such that the four phase gradients can be independently designed. The proposed anisotropic meta-atom contains two identical composite metallic resonators and a continuous metal plate separated by two dielectric spacers (2.5 mm thick F4B board with $\epsilon_r = 2.65 + 0.001i$), see Fig. 2a. To diminish the polarization cross-talking and broaden the bandwidth, we purposely designed the metallic resonator to contain both a metallic cross and an external wire loop. These two structures resonate at two different frequencies. Since the meta-atom is electrically subwavelength (0.277 λ at 10 GHz), the two resonant modes can be quantitatively described by an equivalent circuit model (CM) shown in Fig. 2b, where the lower and upper mode around f_1 and f_2 are physically modeled by a series resonant tank formed by L_1 , C_1 , R_1 , and L_2 , C_2 , R_2 , respectively. Here, L , C and R rep-

resent the effective inductance, capacitance, and resistance (absorption) of the circuit. Figure 2c compares the spectra of reflection phase and amplitude for the single-layer and double-layer meta-atoms (Fig. 2a) based on finite-difference-time-domain (FDTD) calculations. In the single-layer case, two reflection dips are clearly observed around $f_1 = 6.12$ and $f_2 = 9.9$ GHz, resulted from two magnetic resonant modes generated by the couplings between the cross and its surrounding loop with the metallic ground plane, evidenced by the reversed currents on metallic patterns and ground plane as shown in Fig. 2g. Cascading the two resonances appropriately can significantly enhance the working bandwidth. Full-wave simulations (lines) are in good agreements with the CM calculations (symbols). When adding another resonator to form a double-layer meta-atom, couplings between different layers split the two resonances into four (dashed lines in Fig. 2c), and thus the working bandwidth is further enhanced, providing us more freedoms to engineer the phase slope. As depicted in Fig. 2d, changing l_y from 0.5 to 3.65 mm leads to a large phase variation φ_y of near 380° (full 360° cover), while changing l_x has nearly no effects (37° phase shift of φ_y) on the spectra. The latter is highly desired indicating that the y -polarized response of our meta-atom is only sensitive to l_y but is very insensitive to l_x . Symmetry consideration implies that the same conclusion can be drawn if we interchange the indexes x and y .

In contrast, the polarization cross-talking effect is strongly enhanced if we remove the external wire loop from the resonator. As shown in Fig. 2e, in such a case the maximum variation of φ_y is only 161° due to changing l_y but can be as high as 83° due to changing l_x . Obviously, adding an external wire loop can significantly degrade the polarization cross-talking effects. The underlying physics of such an intriguing phenomenon can be understood by checking the field distributions on the cross-bar layers for the resonant modes associated with the $\vec{E} \parallel \hat{y}$ polarization in two different meta-atoms, as shown in Fig. 2g. Due to screening effect of the surrounding wire loop, the excited EM field is more strongly localized to the vicinities of the cross. In particular, the loop-bar coupling generates electric currents on the loop which significantly counteract the currents induced on the x -oriented bar, thereby making the mode rather insensitive to the parameter l_x . In contrast, non-negligible currents always exist on the x -oriented bar in the cross-only meta-atom even for the mode associated with the $\vec{E} \parallel \hat{y}$ polarization, generating the polarization cross-talking. Further calculations (see Supporting Information) indicate that the decrease of w improves the polarization cross-talking property but weakens the capability of phase

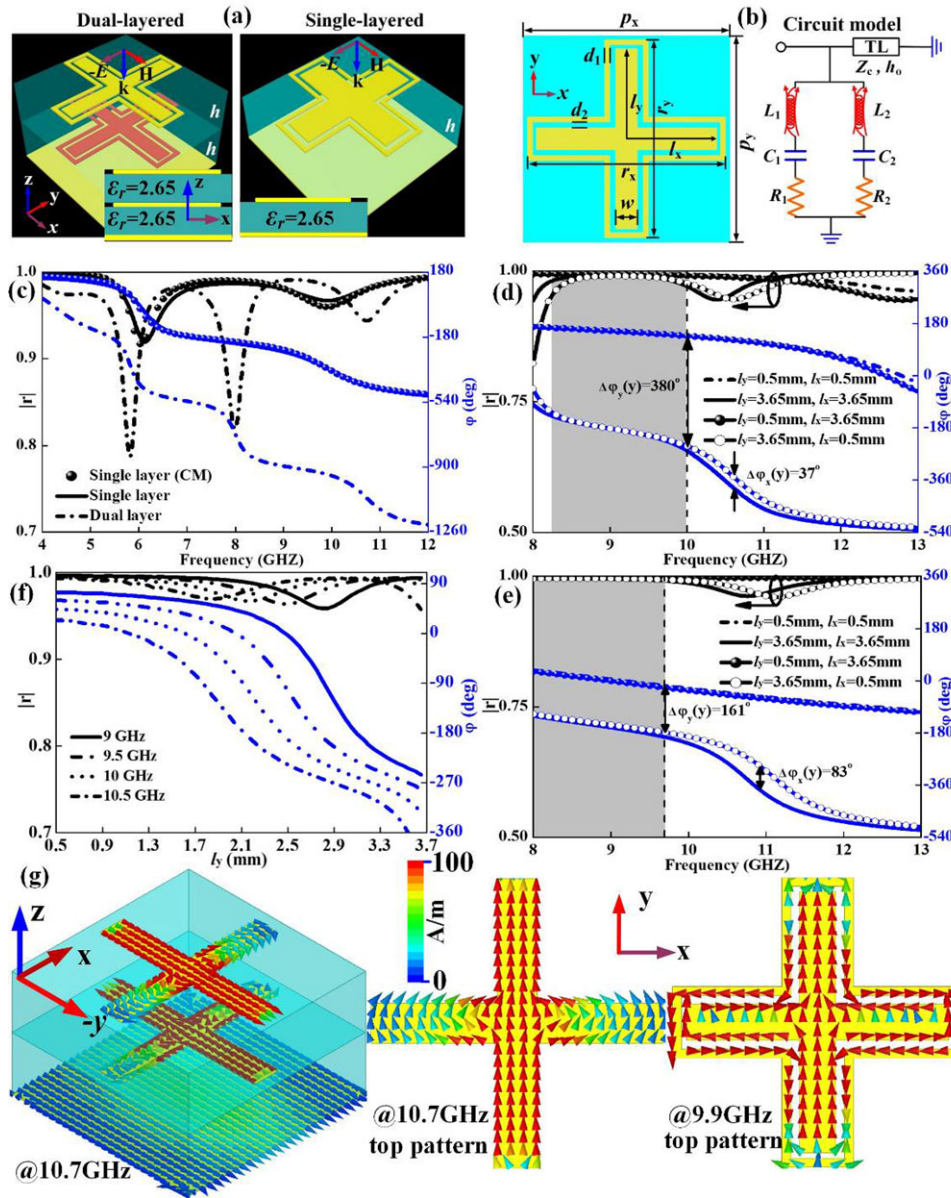


Figure 2 Illustration of the anisotropic meta-atoms without polarization cross-talking. (a) Topology of the dual-layer and single-layer anisotropic meta-atoms using composite cross bar and cross loop. (b) Illustration of geometrical parameters and equivalent circuit model. (c) Reflection coefficients of the single-layer and dual-layer meta-atoms in broad frequency spectrum, the circuit parameters are retrieved as $L_1 = 10$ nH, $C_1 = 0.05$ pF, $L_2 = 0.675$ nH, $C_2 = 0.108$ pF, $R_1 = 2.5$ Ω , $R_2 = 0.31$ Ω , $Z_c = 285.8$ Ω and $h_o = 29.8^\circ$. Reflection coefficients of the dual-layer meta-atoms (d) with and (e) without external wire loop in cases of different l_x and l_y . (f) Reflection coefficients of the dual-layer meta-atoms as a function of l_y at different frequencies of 9, 9.5, 10 and 10.5 GHz when $l_x = 2$ mm. The residual geometrical parameters are $p_x = p_y = 8.3$ mm, $r_x = r_y = 8.1$ mm, $l_x = l_y = 3.65$ mm, $d_1 = d_2 = 0.25$ mm and $w = 1$ mm. All results are calculated under the excitation of y -polarized incident waves. (g) Current distributions on metallic patterns of the cross-only (left and middle panel), and cross-loop dual-layer meta-atoms (right panel).

accumulation. Moreover, it is advisable to select a region far from the resonances to design our meta-atom with highly suppressed polarization cross-talking, as shown by the grey region of Fig. 2d. With the criterion to de-

sign our meta-atom known, we now show the bandwidth performance of the meta-atom. As illustrated in Fig. 2f, the reflection magnitude remains stable and is larger than 0.97 as l_y varies within 0.5~3.65 mm at four

representative frequencies, indicating a satisfactory amplitude uniformity. More importantly, the four phase curves are almost parallel with each other and all exhibit good linear dependences on l_y in a large parameter region. One may easily expect that our meta-atom can work well in all frequencies lying in 9~10.5 GHz, where a full 360° phase coverage and near-unity magnitude can be simultaneously obtained by varying l_y .

3 Bifunctional metasurface design and results

We now employ the proposed anisotropic meta-atom to design a bi-functional metasurface (denoted as sample I) to realize high-gain focused-beam and quad-beam emissions, triggered respectively, by x-polarized and y-polarized free-space excitations. The square metasurface occupies an area of $D \times D = 224 \times 224$ mm² and is fed by a conical horn, see Fig. 3a. It is designed at $f_0 = 10$ GHz and composed of 27×27 anisotropic subwavelength meta-atoms each with a size of 8.3×8.3 mm². For both excitations, the feed is placed $F = 125.5$ mm away from the center of the metasurface (see inset to Fig. 3a and the device topology shown in Supporting Information). The ratio of foci to diameter is $F/D = 0.56$, which is very beneficial to avoid the spillover radiation. To engineer the highly directive focused beam, a parabolic phase profile (Fig. 3c) is necessary which is determined by $\varphi(m, n) = 2\pi(\sqrt{(mp)^2 + (np)^2} + F^2 - F)/\lambda$, where m and n label the position of a specific meta-atom along x and y axes, and F is the focal length. For easy characterization without loss of generality, the four pencil beams are chosen as $\varphi = 0^\circ, 90^\circ, 180^\circ$ and 270° , respectively in both quadbeam syntheses and $\theta = 40^\circ$ in this particular design. Using the alternating projection method (APM) introduced below, we can synthesize the phase profile to exhibit desirable quad-beam emissions.

The finally optimized radiation pattern and phase distribution are shown in Fig. 3b and 3d. Four pencil beams with uniform amplitude and high directivity can be clearly seen from the three-dimensional (3D) radiation pattern of the metasurface (see Fig. 3b). All beams are precisely directed to the angles at $(\varphi_1 = 0^\circ, \theta = 40^\circ)$, $(\varphi_2 = 90^\circ, \theta = 40^\circ)$, $(\varphi_3 = 180^\circ, \theta = 40^\circ)$ and $(\varphi_4 = 270^\circ, \theta = 40^\circ)$, which coincide well with our predetermined target. Moreover, the side-lobe level is below -38 dB, which is quite desirable. The phase distribution of the quad-beam array exhibits two-fold symmetry along x and y directions, yielding a 2D hyperbola-like phase profile with four regions separated by two diagonals (see Fig. 3d). Following the general design procedure devel-

oped for any bifunctional devices in Supporting Information, we can easily determine the metasurface layout by conducting a geometrical mapping process based on a root finding algorithm and phase-parameter database (see Fig. 2f). Thanks to the polarization irrelevance properties of the meta-atom, the geometrical parameters l_x and l_y can be separately determined by two polarization-dependent phase profiles $\varphi_x(x, y)$ and $\varphi_y(x, y)$, respectively. As is shown in Fig. 3a, a 2D distribution of both l_x and l_y across the metasurface is clearly seen.

We fabricated a sample according to the design and characterized its EM performance through both near-field and far-field measurements, utilizing experimental setup shown in Supporting Information. Figures 3e and 3f depict the measured field distributions for E_x and E_y at four representative frequencies. As shown in Fig. 3e, the electric fields reflected from the metasurface are focused to a spot on the x-y plane at all frequencies studied. As such, the different optical paths from the feed to metasurface are precisely collimated. The spot size is obviously decreased as frequency increases due to the shrinking of wavelength. On the other hand, four clear sub-spots with localized intensities are clearly observed in Fig. 3f, reinforcing the quad-beam emissions for the y-polarization observed from the far-field measurements (see Fig. 4). For both single-beam and quad-beam channels, the slightly distorted fields at the low and upper edge frequencies can be attributed to the worsened phases induced by the intrinsic Lorenz dispersions of resonant meta-atoms [20]. The functionalities of our device can be directly seen from Fig. 4a, where FDTD calculated 3D radiation patterns are shown at four representative frequencies. As is expected, we get completely different diagrams for wave-front control under two orthogonal polarizations (two channels). For x polarization (single-beam channel), highly directive pencil beam is clearly seen at all frequencies, where a peak gain of $G = 24.5$ dB is found at $f_0 = 10$ GHz and the aperture efficiency is calculated as 40.2% according to $\eta = \lambda^2 G / 4\pi D^2$. However for y polarization (quadbeam channel), four symmetric pencil beams are clearly inspected at all frequencies studied, with a peak gain of near 17.5 dB at $f_0 = 9.7$ GHz for each beam. Therefore, an aperture efficiency of 33.9% is achieved for quadbeam channel according to $\eta = \lambda^2 \sum_{i=1}^4 G_i / 4\pi D^2$. The feed blockage poses negligible effect to device performance (see Supporting Information), where simulated and measured return loss is better than -12.3 dB across the entire observed band for two polarizations. As shown in Fig. 4b, the gain for single-beam channel is better than 23 dB within 9.2~10.5 GHz. The aperture efficiency varies from 28.4% to 43.3%

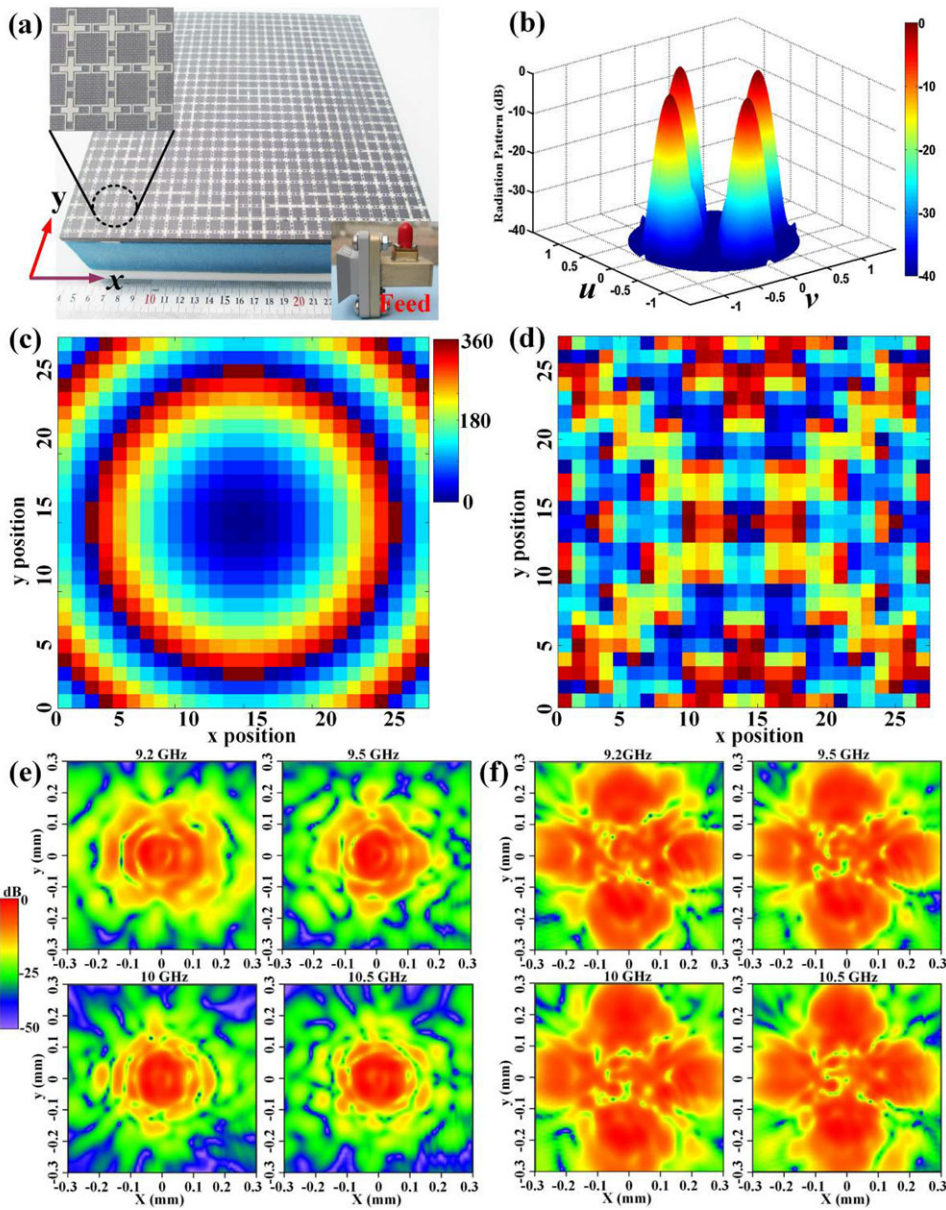


Figure 3 Design and near-field characterization of the bifunctional metasurface I with focused-beam and quad-beam directive emissions. (a) Photograph of the fabricated sample, the inset shows the conical feed horn and zoom-in view of the sample. (b) Theoretically calculated 3D quad-beam radiation patterns at 10 GHz. Objective phase distribution as a function of element position for (c) focused-beam and (d) quad-beam emissions under x-polarized and y-polarized excitations. Measured (e) E_x and (f) E_y distributions (real parts) of the bifunctional metasurface at 9.2, 9.5, 10 and 10.5 GHz in x-y plane under x-oriented and y-oriented polarization, respectively, with the probing waveguide placed 90 mm away from the feed horn. The conical horn with an aperture size of $44 \times 24 \text{ mm}^2$ was designed with 10 dB gain, low sidelobes, and good impedance match at $f_0 = 10 \text{ GHz}$.

and the gain variation is less than $\pm 1 \text{ dB}$, leading to a 1 dB gain bandwidth of 13%. For quad-beam channel, the total gain is better than 22 dB while the gain variation is less than $\pm 1 \text{ dB}$ within 9.4~10.6 GHz, where the aperture efficiency changes from 21% to 32.3%. The spillover loss and scanning loss of each oblique beam account for the rel-

atively lower gain in quad-beam channel. A larger aperture size would be able to narrow the gain gap between these two cases.

Detailed performance of such bifunctional metasurface can be seen from Figs. 4c and 4d where the 2D radiation patterns of our device are shown in x-z (H)

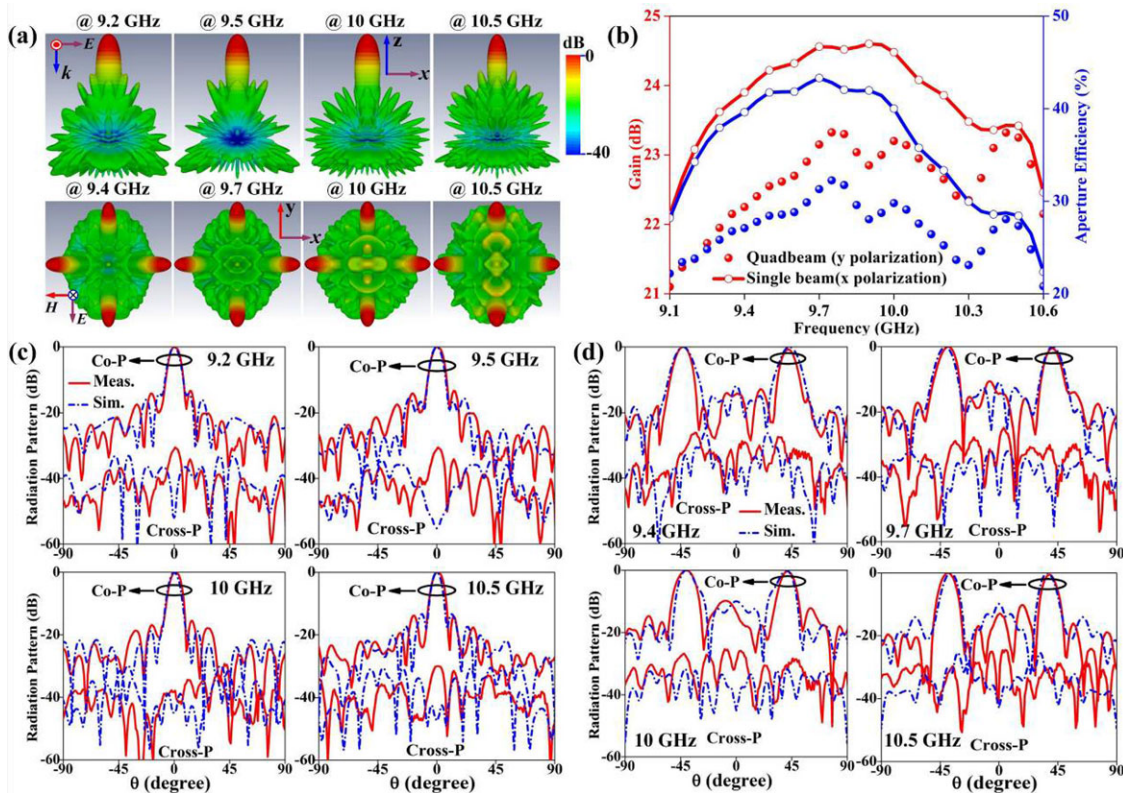


Figure 4 Far-field characterization of the emission system I based on bifunctional metasurface I under x-polarized and y-polarized normally incident plane waves. (a) Side view (top row) and bottom view (bottom row) of the FDTD simulated far-field radiation patterns at four representative frequencies. (b) Measured gain and efficiency, the gain is a sum of four beams in quadbeam channel. (c) Simulated and measured radiation patterns in x-z plane at 9.2, 9.5, 10 and 10.5 GHz for x polarization. (d) Simulated and measured radiation patterns in x-z plane at 9.4, 9.7, 10 and 10.5 GHz for y polarization. Each pattern is normalized to the peak value of the main beam.

plane. Similar y-z (E) plane patterns can be found in Supporting Information. Among all cases, measurements are in reasonable agreement with simulations, further validating our design. For the y-polarization case, we observe two obvious pencil beams efficiently formed in each plane with almost equal intensity (tolerance less than ± 0.54 dB) and desirable symmetry. The half-power beam-width (HPBW) of a typical beam is calculated as $\sim 10^\circ$, which is much less than that of the bare horn ($\sim 55^\circ$). Moreover, the main beam is directed to 44° , 41° , 40° and 38° at 9.4, 9.7, 10 and 10.5 GHz, respectively. Such a frequency dependence of θ is quite physical since the metasurface becomes effectively enlarged in size though its physical size remains unchanged. The side-lobe level around boresight is better than -10.2 dB within 9.4–10.5 GHz and is around -20 dB for most elevation angles. In all cases, the cross polarization is approximately 25 dB lower than the co-polarization peak. For x polarization, a highly directive pencil beam occurring at $\theta = 0^\circ$ is clearly observed at all frequencies studied.

The HPBW is about 7° and the measured cross polarization is less than -29.8 dB in all cases. To sum up, the predicted two functionalities of our metasurface have been unambiguously demonstrated by both simulations and experiments.

We next design another bi-functional metasurface (denoted as sample II) using the same approach and the same type of meta-atoms. For this device, we integrate a linear phase profile and hyperbola-like phase profile into an ultrathin plate to realize two functionalities: beam-steering for x polarization and small-angle quadbeam emissions for y polarization. The steering angle is designed as 37° at 10 GHz by changing l_x while the directions of the quad beams are engineered as $\theta = 30^\circ$ at 10 GHz by changing l_y . Again, the twofold symmetric quadbeam phase distribution is synthesized by utilizing the APM algorithm in Matlab. The linear profile is determined by $\varphi(x) = 2\pi(n-1)p_x \sin \theta / \lambda$, where n is the element number belonging to $[1, N]$ and θ is elevation angle defining beam direction relative to the boresight.

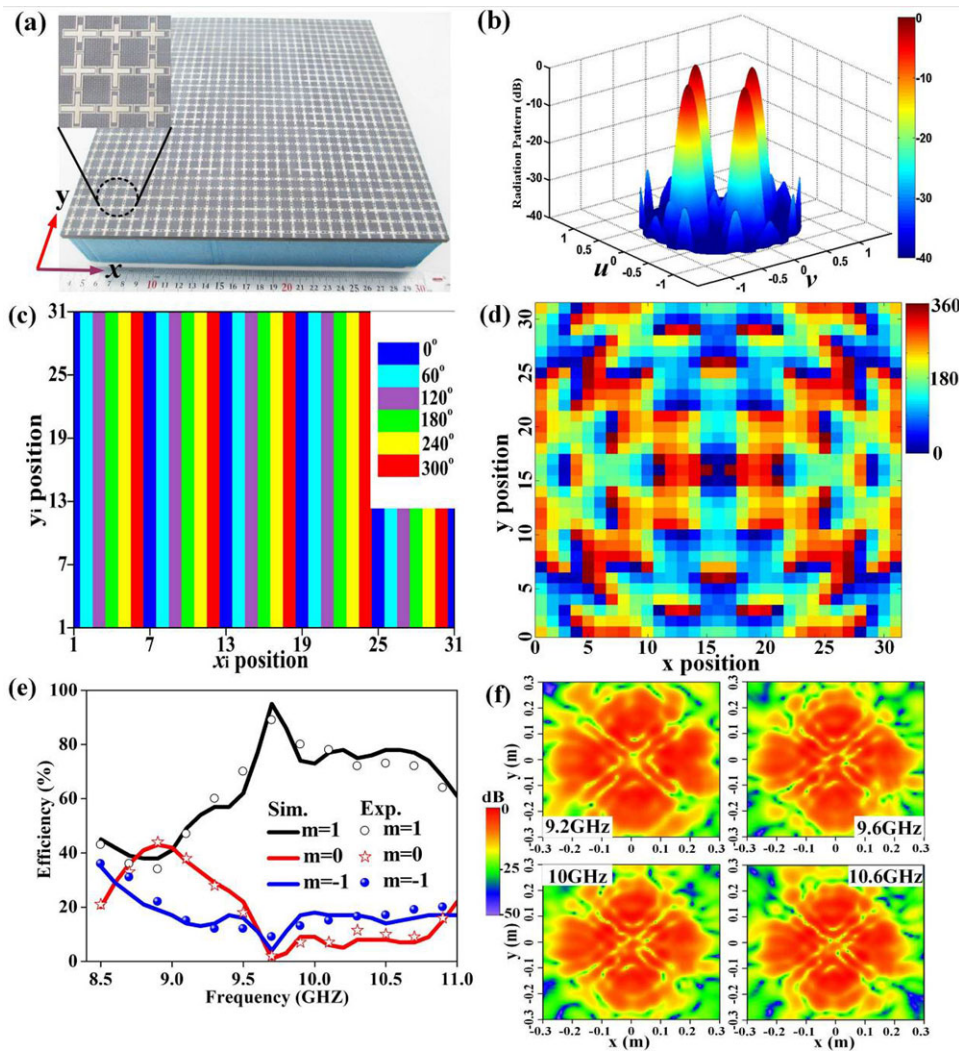


Figure 5 Design and near-field characterization of the bifunctional metasurface II with beam-steering and quad-beam directive emissions. (a) Photograph of the fabricated sample, the inset shows zoom-in view of the sample and the sequentially changed l_x for the linear gradient is 3.65, 3.2, 2.6, 2.31, 2.1 and 1.83mm. (b) Theoretically calculated 3D quad-beam patterns at 10 GHz. Objective phase distribution as a function of element position for (c) beam-steering and (d) quad-beam emissions under x-polarized and y-polarized excitations. (e) Diffraction efficiency of different orders as a function of frequency. The efficiency was defined as the ratio between reflected power ($\int_{-\theta_{-1}/2}^{\theta_{-1}/2} P(\theta) d\theta$, $\int_{\theta_{-1}/2}^{\theta_{1}/2} P(\theta) d\theta$ and $\int_{\theta_{1}/2}^{90^\circ} P(\theta) d\theta$ with θ_{-1} and θ_{1} being the reflection angles of $m = -1$ and $m = 1$ mode) and the totally reflected power ($\int_{-90^\circ}^{90^\circ} P(\theta) d\theta$). (f) Measured E_y distributions (real parts) of the bifunctional metasurface in x-y plane at 9.2, 9.6, 10 and 10.6 GHz under y polarization, with the probing waveguide placed 70 mm away from the feed horn.

The metasurface consist of 31×31 subwavelength meta-atoms and occupies an area of $D \times D = 257.3 \times 257.3$ mm², see Fig. 5a and the device topology shown in Supporting Information. l_x is periodically changed only along x direction, while a 2D change of l_y across the metasurface is clearly seen. For x polarization, a bigger tapered horn with aperture size of 120×90 mm² is positioned at $F_x = 400$ mm away from the metasurface to guarantee an efficient plane-wave excitation. For

y polarization, we used the previously utilized smaller horn to normally shine the metasurface at a distance of $F_y = 154.4$ mm ($F/D = 0.6$). As expected in Fig. 5b, four beams with uniform intensity are achieved along x and y axis, respectively. All beams are precisely directed to $\theta = 30^\circ$ off broadside and all sidelobes are suppressed below -32 dB, indicating an effective design and optimization process. As depicted in Fig. 5c, the designed phases are constant along y direction while are

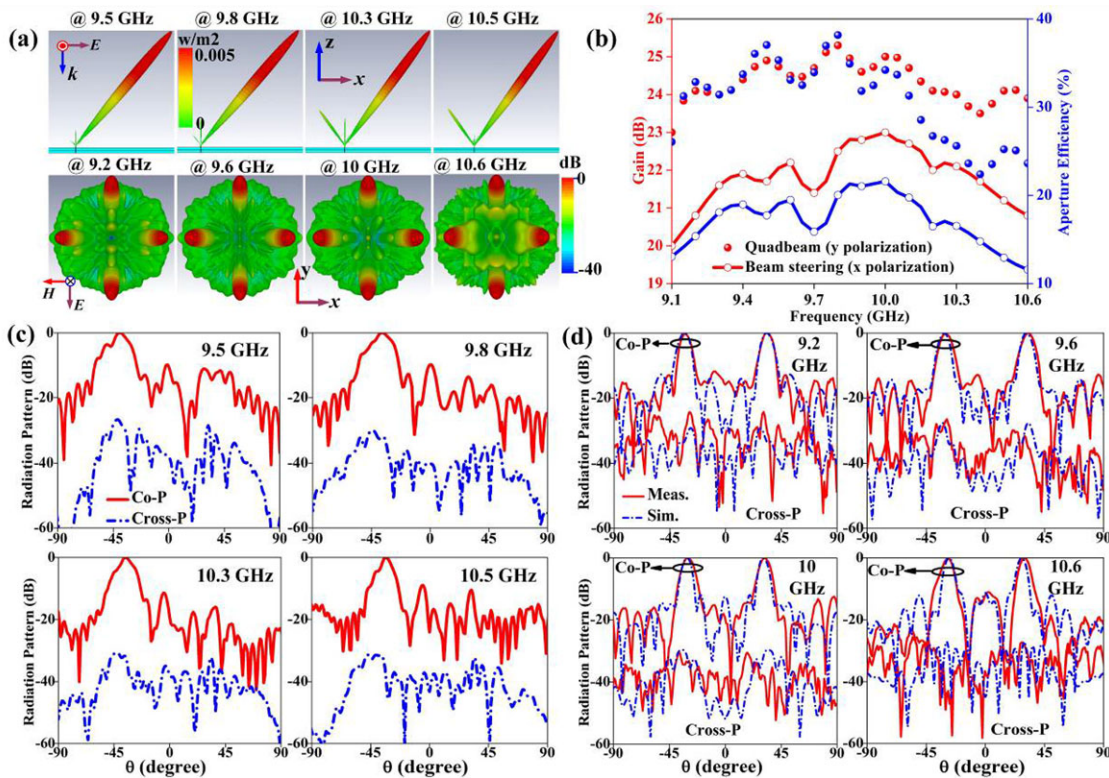


Figure 6 Far-field characterization of the emission system II based on bifunctional metasurface II under x-polarized and y-polarized normally incident plane waves. (a) FDTD simulated far-field radiation patterns at four representative frequencies for x polarization (top row) and y polarization (bottom row). (b) Measured gain and efficiency, the gain is a sum of four beams in quadbeam channel. (c) Measured radiation patterns in x-z plane at 9.5, 9.8, 10.3 and 10.5 GHz under x polarization, here numerical patterns in beam-steering channel are not given due to computational memory constraints. (d) Simulated and measured radiation patterns in x-z plane at 9.2, 9.6, 10 and 10.6 GHz under y polarization. Each pattern is normalized to the peak value of the main beam.

progressively increased along x direction with a constant gradient ($\varphi_{x(i+1)}(x) - \varphi_{x(i)}(x) = 60^\circ$, $i = 1, 2, 3, 4, 5, 6$). The metasurface using such a supercell enables a beam steering behavior predicted by $\theta = \arcsin \lambda_p / 6 p_x$. As shown in Fig. 5d, a hyperbola-like phase profile across the aperture is clearly seen. As expected in Fig. 5e and Figure S6b in Supporting Information, numerical and experimental results coincide well those predicted by the generalized Snell's law [8]. Our device works well within 9.6~10.7 GHz where the anomalous mode ($m = 1$) dominates (the conversion efficiency is more than 72% and the peak efficiency is 95 and 89% in numerical and experimental case at 9.7 GHz) while the normal mode ($m = 0$) and first-order diffraction mode ($m = -1$) are significantly suppressed, corresponding to a bandwidth of 11% relative to $f_0 = 10$ GHz. Such band coincides well with that of metasurface exhibiting only L_x variation, further demonstrating the polarization irrelevance behavior. As portrayed in Fig. 5f, four localized spots with almost uniform E_y field intensities are symmetrically situated on the two axes at

four representative frequencies, accounting for the efficiently synthesized quad pencil beams in far-field region (Fig. 6). Out of the band 9.2–10.6 GHz, these spots become vague in the measured patterns.

Again, the effect of feed blockage to device performance can be negligible since the return loss in both cases is better than -11 dB across the entire band (see Supporting Information). As expected in Fig. 6a, a pure anomalous reflection beam is obtained at all frequencies studied, with both normal and first-order diffraction beams almost completely suppressed. Consequently, a high-gain scanning beam is achieved by placing a feed horn in front of the metasurface. Four pencil beams with symmetric patterns and uniform intensities are observed at a smaller elevation angle. As shown in Fig. 6b, a peak gain (efficiency) of 23 dB (21.6%) is achieved at 10 GHz for x polarization. A variation of gain of less than ± 1 dB is observed from 9.5 to 10.5 GHz, corresponding to a bandwidth of 10%. The gain dips around 9.5, 9.7 and 10.2 GHz is because of the undesired reflection modes induced by

distorted phase profile. These modes tend to direct more energy into sidelobes. Nevertheless, the gain variation is within an acceptable level. For y polarization, the measured gain (aperture efficiency) varies from 23 dB (26.1%) at 9.1 GHz to 23.9 dB (23.7%) at 10.6 GHz with a peak value of 25.3 dB (38.2%) at 9.8 GHz. The relatively lower gain and efficiency in beam-steering channel than that in quadbeam channel are likely caused by the spillover loss due to the finite dimensions of the sample. This is because in former case we placed a bigger horn much farther from the metasurface to guarantee a plane-wave excitation. More power leaked into free space and thus the power captured by the metasurface was reduced. This issue can be substantially addressed by adding more super cells along the aperture which is currently evaluated as 8.58λ at 10 GHz.

The detailed performance of the emission system is further illustrated in Figs. 6c and 6d, where the radiation patterns are plotted in x-z plane in two different polarizations. Similar patterns can be observed in y-z plane, see Supporting Information. From Fig. 6c, we found that the beam-steering angle changes from -39° to -35° as frequency varies from 9.5 to 10.5 GHz. The averaged HPBW is around 13° and the sidelobes are better than -10 dB at most frequencies and the cross polarization is better than -26.7 dB. As shown in Fig. 6d, satisfactory agreement is observed between simulations and measurements at all frequencies studied. Two uniform narrowed beams with almost equal intensity are clearly seen (tolerance less than ± 0.25 dB). The patterns do not change appreciably from 9.2 to 10.6 GHz, indicating a stable and robust multibeam emission. All measured cross polarization is 24.5 dB below the peak intensity. The HPBW is about 8° which is narrower than our first device, thanks to a larger aperture size of present sample.

4 Conclusions

In summary, we proposed an anisotropic meta-atom that exhibits diminished polarization cross-talking, and employed it to efficiently design bifunctional metasurfaces with complicated functionalities requiring 2D parameter optimizations. The key idea is to add a wire loop to isolate the planar resonator and thus to degrade its sensitivity on external environmental changes. As an illustration, we designed and fabricated two bifunctional metasurfaces that integrate different functionalities and experimentally characterized their fascinating wave-manipulation properties. Numerical simulations are in good agreements with the experimen-

tal results, both unambiguously illustrating the desired functionalities. Of particular relevance is the developed design methodology which is general for any bifunctional devices. Our proposal opens an avenue for complex wave front control with high integrity, stability and low cost.

5 APM for quad-beam synthesis

The main procedure of quad-beam synthesis using APM is to search for the intersection between the set of possible radiation patterns (set A) of a metasurface and that of target patterns with idealized performance (set B), based on closed-loop iterative optimizations [44]. The tangential components of the EM field emitted from a metasurface is the sum of waves radiated from different meta-atoms,

$$A \equiv \left\{ T : T(u, v) = \sum_{(m,n) \in I}^N \alpha_{m,n} e^{jk(P_{m,n}^x u + P_{m,n}^y v)} \right\} \quad (3)$$

Here, I is the set of positions of all elements, $u = \sin \theta \cos \varphi$ and $v = \sin \theta \sin \varphi$ are the angular coordinates, $P_{m,n}^x$ and $P_{m,n}^y$ are positions of specific meta-atom along x and y direction, respectively, and $\alpha_{m,n}$ denotes the contribution from the meta-atom located at the position $-m,n$, determined by both the excitation field and the response (reflection amplitude and phase) of the meta-atom itself. The target pattern requirements are specified by two masks, i.e., the multiple pencil beams with uniform amplitude and high gain; and low sidelobes with negligible radiations relative to the peak value. In the first mask, the -3 dB beamwidth and each main beam of target patterns are characterized by the lower and upper bound values ($M_L = 0.707$ and $M_U = 1$),

$$B \equiv \{ T : T(u, v) = M_L(u, v) \leq |T(u, v)| \leq M_U(u, v) \} \quad (4)$$

In the second mask, we define another upper bound M_U at certain elevation angle θ . To minimize the side-lobe level, we require emitted fields in the side-lobe region must fulfill the following requirement,

$$B \equiv \{ T : |T(u, v)| \leq M_U \} \quad (5)$$

The iterative optimization is considered to be converged and will be terminated when the cost function T_{adp} reaches a stable value. In this particular design, M_U is restricted as an achievable value of -30 dB and the

radiation pattern of the feed horn is modeled as $\cos^q(\theta)$ with $q = 8.6$,

$$T_{\text{adp}} = \sum_{u^2+v^2 \leq 1} \sum (|T(u, v)| - M_U)^2 \quad (6)$$

The synthesis consists of projecting the radiation patterns from set A to set B, and projecting the patterns back to the aperture magnitude and phase distribution (inverse Fourier Transform (FFT) algorithms). In the former case, the radiation patterns are rectified progressively until both sets are in good proximity, whereas in the latter case the phase and amplitude of elements across the aperture are dynamically renewed and finally reach the optimum distribution. In reflective scheme, the quad-beam metasurface design is related only to phase synthesis since the element amplitude is determined by aperture size and illumination. Before the phase optimization, one should predetermine some initial parameters such as feed position F relative to metasurface, operation frequency f_0 , aperture size D and element number $N = D/p$, elevation angles θ and azimuth angles φ that defining beam directions.

Acknowledgments. This work was supported by National Natural Science Foundation of China (61501499, 11474057, 61372034, 11174055, 11204040, and 11404063), China Postdoctoral Science Foundation under Grant No. 2015M570323, Special Financial Grant from the China Postdoctoral Science Foundation under Grant No. 2016T90337, MOE of China (Grant No. B06011), Shanghai Science and Technology Committee (Grant No. 14PJ1401200), Natural Science Foundation of Shaanxi Province under Grant 2016JQ6001, and also Aviation Science Foundation of China under Grant No. 20161996009.

Key words. Metasurface, Dual-polarized, Dual-mode, Multifunctional, Highly-directive Emissions.

References

- [1] S. Enoch, G. Tayeb, P. Sabouroux, N. Guérin, and P. Vincent, *Phys. Rev. Lett.* **89**, 213902 (2002).
- [2] Z. H. Jiang, Q. Wu, and D. H. Werner, *Phys. Rev. B* **86**, 125131 (2012).
- [3] H. Xu, G. Wang, and T. Cai, *IEEE Trans. Antennas Propag.* **62**, 3141 (2014).
- [4] N. Kundtz, and D. R. Smith, *Nat. Mater.* **9**, 129 (2010)
- [5] H. F. Ma, and T. J. Cui, *Nat. Commun.* **1**, 124 (2010).
- [6] H. Xu, G. Wang, Z. Tao, and T. J. Cui, *Sci. Rep.* **4**, 5744 (2014).
- [7] N. Engheta, *Science* **334**, 317 (2011).
- [8] N. Yu, P. Genevet, M. A. Kats, F. Aieta, J. P. Tetienne, F. Capasso, and Z. Gaburro, *Science* **334**, 333 (2011).
- [9] S. Sun, Q. He, S. Xiao, Q. Xu, X. Li, and L. Zhou, *Nat. Mater.* **11**, 426 (2012).
- [10] F. Aieta, P. Genevet, N. Yu, M. A. Kats, Z. Gaburro, and F. Capasso, *Nano Lett.* **12**, 1702 (2012).
- [11] N. Yu, and F. Capasso, *Nat. Mater.* **13**, 139 (2014).
- [12] M. Kim, A. M. Wong, and G. V. Eleftheriades, *Phys. Rev. X* **4**, 41042 (2014).
- [13] L. Liu, X. Zhang, M. Kenney, X. Su, N. Xu, C. Ouyang, Y. Shi, J. Han, W. Zhang, and S. Zhang, *Adv. Mater.* **26**, 5031 (2014).
- [14] T. J. Cui, M. Q. Qi, X. Wan, J. Zhao, and Q. Cheng, *Light Sci. Appl.* **3**, e218 (2014).
- [15] F. Aieta, M. A. Kats, P. Genevet, and F. Capasso, *Science* **347**, 1342 (2015).
- [16] X. Zhang, Z. Tian, W. Yue, J. Gu, S. Zhang, J. Han, and W. Zhang, *Adv. Mater.* **25**, 4567 (2013).
- [17] N. K. Grady, J. E. Heyes, D. R. Chowdhury, Y. Zeng, M. T. Reiten, A. K. Azad, A. J. Taylor, D. A. R. Dalvit, and H. T. Chen, *Science* **340**, 1304 (2013).
- [18] F. Monticone, N. M. Estakhri, and A. Alù, *Phys. Rev. Lett.* **110**, 203903 (2013).
- [19] F. Qin, L. Ding, L. Zhang, F. Monticone, C. C. Chum, J. Deng, S. Mei, Y. Li, J. Teng, and M. Hong, *Science advances* **2**, e1501168 (2016).
- [20] H. Xu, S. Tang, S. Ma, W. Luo, T. Cai, S. Sun, Q. He, and L. Zhou, *Sci. Rep.* **6**, 38255 (2016).
- [21] A. Pors, M. G. Nielsen, R. L. Eriksen, and S. I. Bozhevolnyi, *Nano Lett.* **13**, 829 (2013).
- [22] F. Aieta, P. Genevet, M. A. Kats, N. Yu, R. Blanchard, Z. Gaburro, and F. Capasso, *Nano Lett.* **12**, 4932 (2012).
- [23] X. Ni, S. Ishii, A. V. Kildishev, and V. M. Shalaev, *Light Sci. Appl.* **2**, e72 (2013).
- [24] X. Chen, M. Chen, M. Q. Mehmood, D. Wen, F. Yue, C. Qiu, and S. Zhang, *Adv. Opt. Mater.* **3**, 1201 (2015).
- [25] N. Yu, F. Aieta, P. Genevet, M. A. Kats, Z. Gaburro, and F. Capasso, *Nano Lett.* **12**, 6328 (2012).
- [26] P. Genevet, N. Yu, F. Aieta, J. Lin, M. A. Kats, R. Blanchard, M. O. Scully, Z. Gaburro, and F. Capasso, *Appl. Phys. Lett.* **100**, 13101 (2012).
- [27] M. Q. Mehmood, S. Mei, S. Hussain, K. Huang, S. Y. Siew, L. Zhang, T. Zhang, X. Ling, H. Liu, and J. Teng, *Adv. Mater.* **28**, 2533 (2016).
- [28] J. Lin, J. P. B. Mueller, Q. Wang, G. Yuan, N. Antoniou, X. C. Yuan, and F. Capasso, *Science* **340**, 331 (2013).
- [29] Z. Wang, H. Jia, K. Yao, W. Cai, H. Chen, and Y. Liu, *Acs Photonics* **3**, 2096 (2016).
- [30] X. Ni, A. V. Kildishev, and V. M. Shalaev, *Nat. Commun.* **4**, 2807 (2013).
- [31] L. Huang, X. Chen, H. Mühlendernd, H. Zhang, S. Chen, B. Bai, Q. Tan, G. Jin, K. Cheah, C. Qiu, J. Li, T. Zentgraf, and S. Zhang, *Nat. Commun.* **4**, 2808 (2013).
- [32] G. Zheng, H. Mühlendernd, M. Kenney, G. Li, T. Zentgraf, and S. Zhang, *Nat. Nanotechnol.* **10**, 308 (2015).
- [33] A. Pors, O. Albrechtsen, I. P. Radko, and S. I. Bozhevolnyi, *Sci. Rep.* **3**, 2155 (2013).
- [34] H. F. Ma, G. Z. Wang, G. S. Kong, and T. J. Cui, *Sci. Rep.* **5**, 9605 (2015)
- [35] W. Luo, S. Xiao, Q. He, S. Sun, and L. Zhou, *Adv. Opt. Mater.* **3**, 1102 (2015).

- [36] M. A. Kats, P. Genevet, G. Aoust, N. Yu, R. Blanchard, F. Aieta, Z. Gaburro, and F. Capasso, Proceedings of the National Academy of Sciences **109**, 12364 (2012).
- [37] C. Pfeiffer, C. Zhang, V. Ray, L. J. Guo, and A. Grbic, Phys. Rev. Lett. **113**, 23902 (2014).
- [38] R. Quarfoth, and D. Sievenpiper, IEEE Trans. Antennas Propag. **62**, 4143 (2014).
- [39] S. Liu, T. J. Cui, Q. Xu, D. Bao, L. Du, X. Wan, W. X. Tang, C. Ouyang, X. Y. Zhou, H. Yuan, H. F. Ma, W. X. Jiang, J. Han, W. Zhang, and Q. Cheng, Light Sci. Appl. **5**, e16076 (2016).
- [40] H. Xu, S. Sun, S. Tang, S. Ma, Q. He, G. Wang, T. Cai, H. Li, and L. Zhou, Sci. Rep. **6**, 27503 (2016).
- [41] Y. B. Li, B. G. Cai, Q. Cheng, and T. J. Cui, Adv. Funct. Mater. **26**, 29 (2016).
- [42] R. Florencio, J. A. Encinar, R. R. Boix, V. Losada, and G. Toso, IEEE Trans. Antennas Propag. **63**, 1234 (2015).
- [43] S. V. Hum, J. Perruisseau-Carrier, *Antennas and Propagation*, IEEE Trans. Antennas Propag. **62**, 183 (2014).
- [44] P. Nayeri, F. Yang, and A. Z. Elsherbeni, *Antennas and Propagation*, IEEE Trans. Antennas Propag. **60**, 1166 (2012).

Supporting Information

Additional supporting information may be found in the online version of this article at the publisher's website.